



A large-eddy simulation study on the similarity between free vibrations of a flexible cylinder and forced vibrations of a rigid cylinder

Zhicheng Wang^{a,1}, Dixia Fan^{b,1}, Michael S. Triantafyllou^{b,*},
George Em Karniadakis^a

^a Brown University, Providence, RI 02912, USA

^b Massachusetts Institute of Technology, Cambridge, MA 02139, USA

ARTICLE INFO

Article history:

Received 3 April 2020

Received in revised form 26 November 2020

Accepted 6 January 2021

Available online xxxx

Keywords:

Vortex-induced vibration

Large-eddy simulation

Strip theory

ABSTRACT

The strip theory in hydrodynamics has been widely used for predicting complex vortex induced vibrations (VIV) behind bluff bodies, but the question of how accurate such predictions are has not been addressed adequately before. In order to corroborate the application of strip theory in VIV, we present a comparative study between free mono-frequency vibrations of a long flexible cylinder in both uniform and linearly sheared flow and corresponding forced vibrations of a rigid cylinder with prescribed sinusoidal motions. We employ the entropy-viscosity large-eddy simulation (LES) to resolve the vortical flow and the coupled cylinder response, which we validate by companion experiments of the same configuration. We then extract from LES, at the same Reynolds number, the values of the sectional vibration amplitude, frequency, and phase angle (between inline and crossflow motions), and use them as input parameters for the forced vibration case, for which we perform *two-dimensional* simulations. We show here by systematic simulation studies that the hydrodynamic coefficients exhibit strong similarities between the two cases, and the *forced vibration* closely resembles the sectional near wake of the *free vibration*.

© 2021 Elsevier Ltd. All rights reserved.

1. Introduction

The vortex-induced vibration (VIV) of a circular cylinder is of great interest due to its importance in the design and operation in a wide range of engineering applications, such as marine risers oscillating in the ocean, bridges, heat exchangers, and even cables in electric networks. In the offshore industry, VIV of marine risers may lead to severe structural fatigue damage (Zheng et al., 2014b), therefore a great amount of research has focused on better understanding and predicting the VIV response as well devising suppressing methods, e.g. streaks, to mitigate the excessive fatigue damage (Fan et al., 2017).

In general, the VIV prediction methods can be categorized into two approaches: the empirical/semi-empirical models and the computational fluid dynamics (CFD). The major difference between them is on how they describe the flow characteristics and corresponding hydrodynamic forces on cylinders (Gabbai and Benaroya, 2005). Specifically, the first

* Corresponding author.

E-mail address: mistetri@mit.edu (M.S. Triantafyllou).

¹ Contributed equally.

approach applies strip theory (Wu et al., 2012) and predicts the VIV response by employing the hydrodynamic coefficients from the experimental database, while the second approach calculates the VIV response by solving the coupled problem of a vibrating cylinder and ambient fluid flow together. In general, the CFD approach yields more accurate predictions, but due to the extensive computational resources required for the CFD, even today in the era of exaflop computing, the offshore industry still relies heavily on the semi-empirical prediction tools, such as the formulations in codes like Shear 7 (Vandiver, 1999), VIVA (Triantafyllou et al., 1999) and VIVANA (Larsen et al., 2001).

The database employed in these semi-empirical prediction codes is mainly obtained from experiments on forced vibrations of rigid cylinders (Sarpkaya, 1978). In such experiments, a rigid cylinder is forced to vibrate in the cross-flow (CF) direction and possibly in the in-line (IL) direction with sinusoidal trajectories at prescribed frequencies and amplitudes. With controlled cylinder motion and measured fluid forces, the corresponding hydrodynamic coefficients can be obtained, such as the mean drag coefficient C_d , the lift/drag coefficient in-phase with the velocity C_{lv}/C_{dv} , and the added mass coefficient in the CF/IL direction C_{my}/C_{mx} , namely the component in the lift/drag force in-phase with the acceleration.

One of the first and most comprehensive set of experiments on CF-only forced vibration of a rigid cylinder was performed in the MIT Towing Tank facility (Gopalkrishnan, 1993) with varying non-dimensional parameters of the true reduced velocity $V_r = \frac{U_\infty}{fD}$ and non-dimensional CF amplitude $\frac{A_y}{D}$, where U_∞ is the prescribed fluid velocity, f is the prescribed motion frequency, A_y is the prescribed motion amplitude and D is the cylinder diameter. The findings from these experiments revealed that regions of positive C_{lv} , indicating net energy transferred from the fluid to structure over one motion period, were located in a certain range of V_r and $\frac{A_y}{D}$. In addition, it was found that the added mass coefficient could vary significantly from a negative value to a large positive value around the true reduced velocity $V_r = 5.9$. The importance of the aforementioned measured hydrodynamic coefficients is that they provide accurate predictions of the rigid cylinder VIV in the CF direction (Wang et al., 2003), and indeed they have served as databases for fluid forces for multiple semi-empirical prediction tools. Later, this hydrodynamic database was extended to include the effects of the IL amplitude and the phase angle θ between the IL and the CF trajectory. The experiments on forced vibration of rigid cylinders in both CF and IL directions were performed by Dahl (2008), Zheng et al. (2014a), and the results showed that the phase angle θ has a strong influence on the fluid forces, and favorable positive energy-in ($C_{lv} > 0$) was strongly associated with θ corresponding to a counter-clockwise (CCW) trajectory (Dahl et al., 2007, 2010).

Nonetheless, the application of the hydrodynamic coefficient database to any semi-empirical prediction model depends on a fundamental assumption of strip theory, which states that the fluid forces, and hence the wake pattern as well, of the flexible cylinder at each cross-section along the cylinder span is similar to the forced vibration of a rigid cylinder at similar conditions. Several researchers have experimentally studied the fluid force distribution along the flexible cylinder via inverse methods and compared with that from the experiments of forced vibration of rigid cylinders (Huarte et al., 2006; Tang et al., 2011; Wu, 2011; Han et al., 2018). Specifically, the experiments in Carberry et al. (2003, 2005) revealed a remarkable similarity in the wake modes between the forced vibration and free vibration. However, due to the insufficient measurement data and the experimental errors, the experimental results could only provide some qualitative insights (Tang et al., 2011).

Meanwhile, some progress was made by the CFD approach to address the aforementioned similarity. A series of high-fidelity DNS studies were presented in Newman and Karniadakis (1996, 1997), Evangelinos and Karniadakis (1999), Evangelinos et al. (2000) using the spectral element method for simulating VIV of a flexible cylinder with aspect ratio of 4π in uniform flow at Reynolds numbers 100, 200 and 1000. Specifically, the structural response and the hydrodynamic force distributions were reported in order to connect the VIV of flexible cylinders to the forced vibration of rigid cylinders. In particular, (Blackburn et al., 2000) presented a direct comparison between DNS and the experiments of Govardhan and Williamson (2000). Moreover, (Bourguet et al., 2011) confirmed that the θ values of the counter-clock wise (CCW) trajectory along the flexible cylinder were also favorable to the positive energy-in from fluid to structure, which agrees with that of the forced vibration of rigid cylinders (Dahl et al., 2007).

More recently, we have used an underwater optical tracking system to reconstruct the sectional fluid forces in a flexible cylinder, and compared them with the rigid cylinder hydrodynamic database (Fan et al., 2019). We concluded that employing strip theory with the hydrodynamic coefficients obtained from forced rigid cylinder experiments could predict the distributed forces accurately. However, the relevance of the vortex shedding pattern between the free vibrating flexible cylinder and the forced vibrating rigid cylinder could not be answered. To this end, in the current work, we first employ the entropy-viscosity method (EVM) to perform large-eddy simulations (LES) of VIV of a flexible cylinder in both uniform and linearly sheared current, and we validate them by our companion experiments in uniform flow at exactly the same set of structural (mass and damping ratio) and flow parameters (Reynolds number Re). Subsequently, we conduct *two-dimensional* simulations of a rigid cylinder undergoing prescribed motions with amplitude and frequency taken from the *free vibration*. Finally, we examine the similarity of the hydrodynamic coefficients and wake patterns between the *free vibration* and the *forced vibration*.

The rest of the paper is organized as follows. In Section 2 we present the numerical methods and simulation parameters. In Section 3 we present the numerical results emphasizing the strong connection between *free vibration* and *forced vibration*. In Section 4 we summarize the main findings of this paper. In the Appendices, we provide details on the validation of the simulation results by our experiments.

2. Numerical method and model

In this paper, both the *free vibration* and *forced vibration* simulations are performed by employing the entropy–viscosity method (EVM), which was originally proposed by [Guermond et al. \(2011a,b\)](#), and further extended in [Wang et al. \(2019, 2018\)](#). In particular, the mixed spectral-element/Fourier method, with spectral-element discretization on the $(x - y)$ plane and Fourier expansion along the cylinder axial direction (z) is used to discretize the incompressible Navier–Stokes equations ([Karniadakis and Sherwin, 2005](#)). The boundary deformation due to the vibration is taken into account by a coordinate transformation method first proposed in [Newman and Karniadakis \(1997\)](#). Note that after taking the Fourier expansion, the *three-dimensional* flow problem is transformed into a series of *two-dimensional* computations, which can significantly reduce the computing time, plus the nonlinear step where FFTs are employed for efficiency.

For the LES of the *free vibration* subject to uniform flow, the computational domain has a size of $[-6.5D, 23.5D] \times [-20D, 20D]$ on the $(x - y)$ plane with a spanwise length $240D$, which is the same as that of the experiment in [Fan et al. \(2019\)](#), [Fan \(2019\)](#). Here $D = 1$ is the diameter of the cylinder, whose center is placed at $(0, 0)$. On the left boundary of the domain where $x/D = -6.5$, a uniform inflow profile, i.e., $u = U$, $v = 0$, $w = 0$, is imposed, where u , v , w are the three components of the velocity vector \mathbf{u} . On the right boundary where $x/D = 23.5$, $p = 0$ and $\frac{\partial \mathbf{u}}{\partial \mathbf{n}} = 0$ are prescribed, where p is the pressure and \mathbf{n} is the normal vector. On both top and bottom boundaries where $y/D = \pm 20$, a periodic boundary condition is used. Furthermore, the domain on the $(x - y)$ plane is partitioned into 2616 quadrilateral elements clustered around the cylinder in order to resolve the boundary layer. Specifically, on the radial direction, the size of the first layer element around the cylinder is $0.01D$, which gives rise to $y^+ < 1$ in all the simulations of this paper. The resolution along the azimuthal direction, in terms of element edge length, is $\frac{\pi D}{64}$. Note that the *two-dimensional* simulations of the *forced vibration* are based on the same computational domain and mesh partition on the (x, y) plane.

Following the convention of the VIV literature, we define the following two reduced velocities,

$$U_r = \frac{U_\infty}{f_{n1}D}, \quad V_r = \frac{U_\infty}{f_y D}, \quad (1)$$

where $f_{n1} = \frac{1}{2L} \sqrt{\frac{\bar{T}}{(m^* + C_m) \frac{\rho \pi d^2}{4}}}$ is the first modal natural frequency, calculated based on the measured tension, where \bar{T} is the average tension along the span, ρ is the fluid density and assuming the added mass coefficient is $C_m = 1.0$ along the model, and f_y is the actual vibration frequency measured in the CF direction. For the *free vibration*, the cylinder motion is governed by the following equation,

$$\frac{\partial^2 \xi_J}{\partial t^2} + 2\zeta \omega_n \frac{\partial \xi_J}{\partial t} + \frac{EI}{\mu} \frac{\partial^4 \xi_J}{\partial z^4} - \frac{\partial}{\partial z} \left(\frac{T}{\mu} \frac{\partial \xi_J}{\partial z} \right) = \frac{C_J}{2\mu}, \quad (2)$$

where ξ_J is the displacement along the J -direction ($J = x$ or $J = y$), and μ is the cylinder mass per unit length. The damping coefficient $\zeta = 8.7\%$ is equal to that of experiment with $\omega_n = 2\pi \frac{U_\infty}{U_r D}$, and EI is the bending stiffness. Note that of the experiment ([Fan et al., 2019](#)), the riser is placed vertically, which leads to a linearly varying tension from the bottom end to the top end of the cylinder, therefore here in the current LES, a linear function of z for T is employed, as given below,

$$T = T_{\max} - \frac{T_{\max} - T_{\min}}{L} z, \quad (3)$$

where $T_{\max} = \frac{T'_{\max}}{T_m} T_m$ and $T_{\min} = \frac{T'_{\min}}{T_m} T_m$. Here T_{\max} , T_{\min} and T_m are the maximum, minimum and mean values of the tension used in simulation. Same as those in the experiment ([Fan et al., 2019](#)), $T'_{\max} = 1.33 T'_{\min}$, $T'_m = 0.5(T'_{\max} + T'_{\min})$, and using $T_m = (2.0 * \frac{U_\infty}{U_r D} L)^2 (\mu + \frac{\pi}{4})$, we can obtain T along the cylinder span. Note that in the experiments, $EI < 0.01T$, while the exact value is changing case by case. In current simulations, $EI = 0.02 T_m$ ensures that the riser is tension dominated, see [Evangelinos and Karniadakis \(1999\)](#). C_J is the J -component of the hydrodynamic force coefficient exerted on the cylinder surface. Eq. (2) is constrained by the pinned boundary condition ($\xi_J = 0$ and $\frac{\partial^2 \xi_J}{\partial z^2} = 0$) at both ends.

For the LES of the *free vibration* in linearly sheared flow, the computational domain and mesh on the $(x - y)$ plane are the same as those of uniform flow. However, in order to take the advantage of FFTs, in the spanwise direction, the domain size ($z/L \in [0, 240]$) is extended by 10% ($z/L \in (240, 267]$), where the buffer layer is set to recover the periodicity, which is explained in detail by [Bourguet et al. \(2013a\)](#). It is worth noting that in our simulation, for the structure Eq. (2) an additional pinned constraint is placed at $z/L = 240$.

In total, we performed 8 simulations of the *free vibrations* subject to uniform inflow of U_r in the range of $[10.75, 17.22]$, and we present validation tests on displacements and excited frequencies in [B](#). In addition, 2 simulations of the *free vibrations* in linearly sheared current at $U_r = 15.65$ are conducted. Note that, here in the case of linearly sheared flow, $U_r = \frac{U_m}{f_{n1}D}$, where $U_m = (U_{\max} + U_{\min})/2$ is the mean inflow velocity. U_{\max} and U_{\min} are the highest and lowest inflow velocity, respectively. Specifically, $U_{\max} = 1.4U_\infty$, $U_{\min} = 0.6U_\infty$ and $U_{\max} = 1.375U_\infty$, $U_{\min} = 0.625U_\infty$ are used in the two cases of linearly sheared current, respectively, and the result of the former will be presented in the main text, while the latter will be summarized in [C](#). In both cases, $Re = U_m D/\nu = 800$, where ν is the kinematic viscosity.

Table 1

Key simulation parameters for the simulations of flow past a uniform flexible cylinder.

Model parameters	Values
Diameter D	1
Aspect ratio L/D	240
Mass ratio m^*	4.0
Damping ratio ζ	8.7%
Simulation case	
Reynolds number Re	550–900
Reduced velocity U_r	10.75–17.22

Eq. (2) is discretized by the 2nd order central-difference scheme in space and the Runge–Kutta method in time. For all the simulations of the *free vibrations* and *forced vibrations* in this paper, unless mentioned explicitly, we employ three spectral-element modes in each element on the (x, y) plane. For the LES of *free vibration* in uniform current, we use 512 Fourier planes along the axis (z -direction), while for the cases of linearly sheared current, we use 576 Fourier planes. Note that in order to minimize the aliasing error, we employ over-integration, i.e., we use 5-points Gauss–Lobatto quadrature in each element and the 3/2 de-aliasing rule in the Fourier direction. For each simulation, the total computational time $\frac{U_\infty}{D} \geq 500$ with a time step $\frac{\Delta t U_\infty}{D} = 1.5 \times 10^{-3}$, which results in the CFL number less than 1.2. For the parameters α and β of EVM, we have followed the rule established in our previous studies (Wang et al., 2018, 2019), namely $\alpha = 0.5$ and $\beta = 0.5$ are used in all our simulations of this paper. We present some of the key physical parameters in Table 1.

Recall that in the widely used semi-empirical models based on the strip theory (Newman, 2018), it is assumed that the sectional force and wake along the flexible cylinder at each location resemble those of the forced vibration of a rigid cylinder in the open flow at the same Re . To corroborate this assumption, we systematically performed dozens of simulations of the *forced vibration*, with the cylinder motions in CF and IL direction given by the following equations,

$$Y(t) = \frac{A_y}{d} \cos(\omega t), \quad X(t) = \frac{A_x}{d} \cos(2\omega t + \theta), \quad (4)$$

where the values of $\frac{A_x}{d}$, $\frac{A_y}{d}$, ω and θ are taken from the simulation results of the two cases of the *free vibrations*: $U_r = 12.66$ ($Re = 650$) and $U_r = 13.61$ ($Re = 700$), shown in Figs. 1 and 2, respectively. In total, for the case of uniform inflow, we simulated 36 sectional planes of the former and 40 of the latter case using Eq. (4). For the two cases of linearly sheared flow, we simulated 40 sectional planes. Note that the locations of sectional planes are equally spaced along the flexible cylinder.

3. Simulation results and discussion

3.1. Free vibration: motions and fluid force distributions

The simulation results for frequency (f), amplitude ($1/10^{\text{th}}$ highest peak) response (A) and the phase between the IL and the CF trajectory (θ) along the cylinder span are plotted in Fig. 1 of uniform flow for $U_r = 12.66$ ($Re = 650$), in Fig. 2 of uniform flow for $U_r = 13.61$ ($Re = 700$) and in Fig. 3 of linearly sheared flow for $U_r = 15.65$ ($Re = 800$). First of all, as shown in the three figures, in both uniform and linearly sheared current, the cylinder response frequency is single narrow-banded in the CF direction (subfigure (a)), while in the IL direction (subfigure (b)), although there are additional frequency components, the exact 2nd harmonic vibration dominates the response. However, even for the two cases of uniform flow at different reduced velocities, the amplitude response and phase response exhibit quite different characteristics. In Fig. 1(c) at $U_r = 12.66$, the flexible cylinder vibrates at the 4th mode in the IL direction and at the 2nd mode in the CF direction, while at $U_r = 13.61$ shown in Fig. 2(c), it vibrates at the 5th mode in the IL direction and at the 3rd mode in the CF direction. Moreover, for the case of $U_r = 13.61$ in Fig. 2(d), the phase response along the span shows a pure standing wave pattern, with the magnitude of θ kept relatively constant in the half wavelength of the IL mode and a jump of 180 degrees at the IL nodes. In contrast, for the case of $U_r = 12.66$ in Fig. 1(d), a traveling wave response develops in the CF direction, and instead of being a constant value θ varies continuously in the half wavelength of the IL mode. For the case of linearly sheared flow at $U_r = 15.65$ with $U_{\max} = 1.4U_\infty$ and $U_{\min} = 0.6U_\infty$, as shown in Fig. 3(c), the flexible cylinder vibrates at the 6th mode in the IL direction and at the 3rd mode in the CF direction. In Fig. 3(d), strong traveling wave response could be observed in the CF direction, and the value of θ varies continuously in the half wavelength of the IL mode. Note that such observation of θ is similar to the findings obtained in the analysis in Bourguet et al. (2013b).

The frequency components of the C_l and C_d signals along the flexible cylinder at $U_r = 12.66$ are plotted in Fig. 4(a) and Fig. 4(b), respectively. We observe that C_l along the span not only exhibits the 1st harmonic but also a strong 3rd harmonic term. The 2nd harmonic dominates C_d , but weak 1st and 3rd harmonic terms can also be observed. Note that the time trace of the sectional C_l and C_d at $z/d = 0.395$ (denoted in Fig. 4(a) and (b) with black dashed line) are plotted in

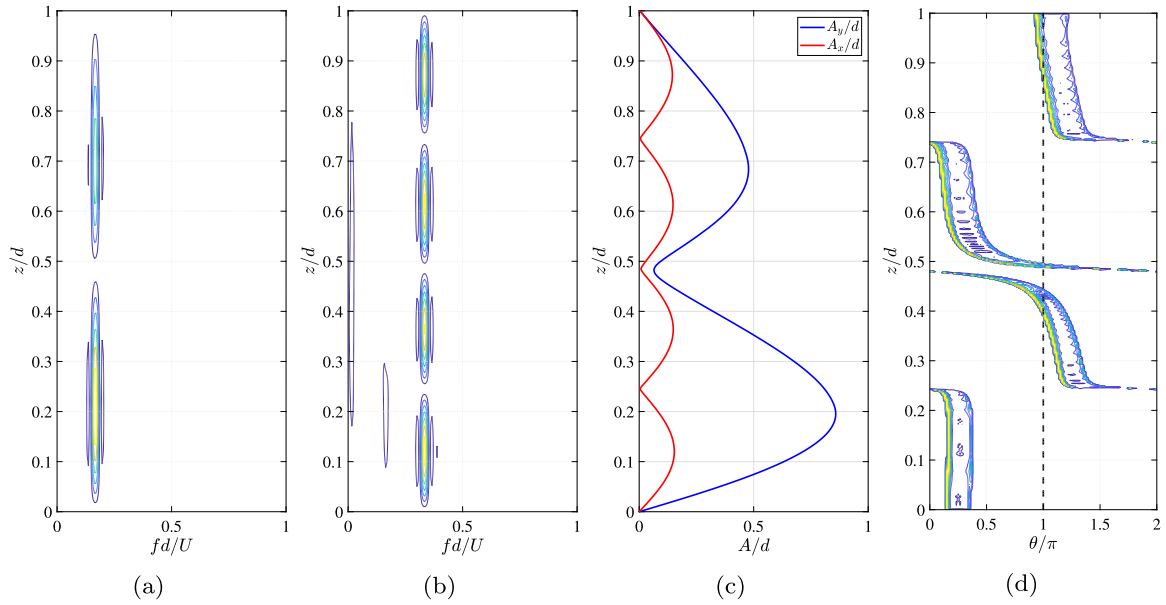


Fig. 1. Free vibration: structural response along the cylinder span at $U_r = 12.66$, $Re = 650$: (a) CF frequency; (b) IL frequency; (c) IL (red) and CF (blue) amplitudes; (d) phase angle θ . (For interpretation of the references to color in this figure legend, the reader is referred to the web version of this article.)

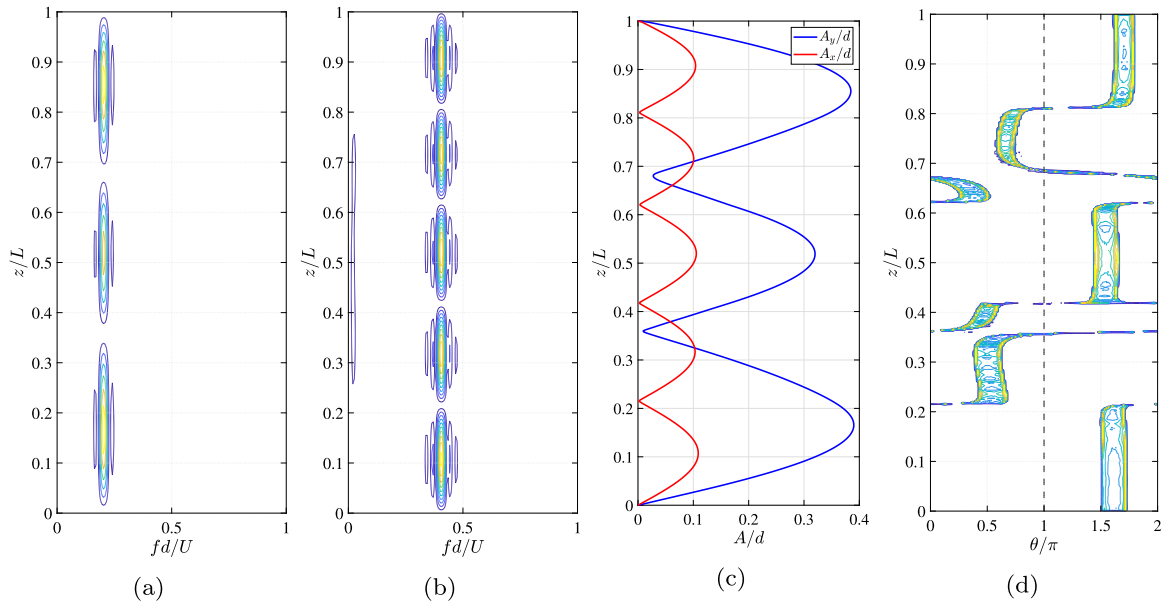


Fig. 2. Free vibration: structural response along the cylinder span at $U_r = 13.61$, $Re = 700$. See Fig. 1 for the caption of each subfigure.

Fig. 4(c) and (d) for C_l and C_d , respectively. Fig. 5 shows the corresponding results from the simulation of linearly sheared current at $U_r = 15.65$ with $U_{max} = 1.4U_\infty$ and $U_{min} = 0.6U_\infty$, very similar behavior of C_l and C_d are observed, despite the fact that notable traveling waves exist along the entire cylinder span.

3.2. Comparison between the forced vibration and the free vibration: hydrodynamic coefficients and wake patterns

Knowing the vibration response and the fluid forces, the widely used hydrodynamic coefficients in VIV community, namely the fluid coefficient in phase with velocity C_v (C_{lv} in the CF direction and C_{dv} in the IL direction) and the added

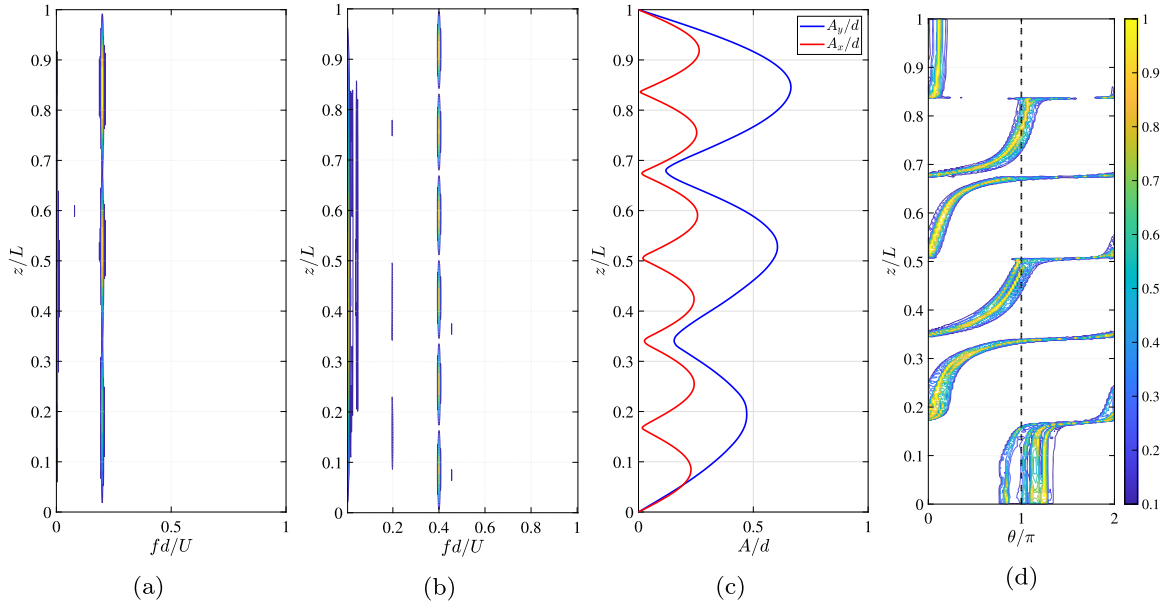


Fig. 3. Free vibration in linearly sheared current at $U_r = 15.65$ with $U_{max} = 1.4U_\infty$ and $U_{min} = 0.6U_\infty$. See Fig. 1 for the caption of each subfigure.

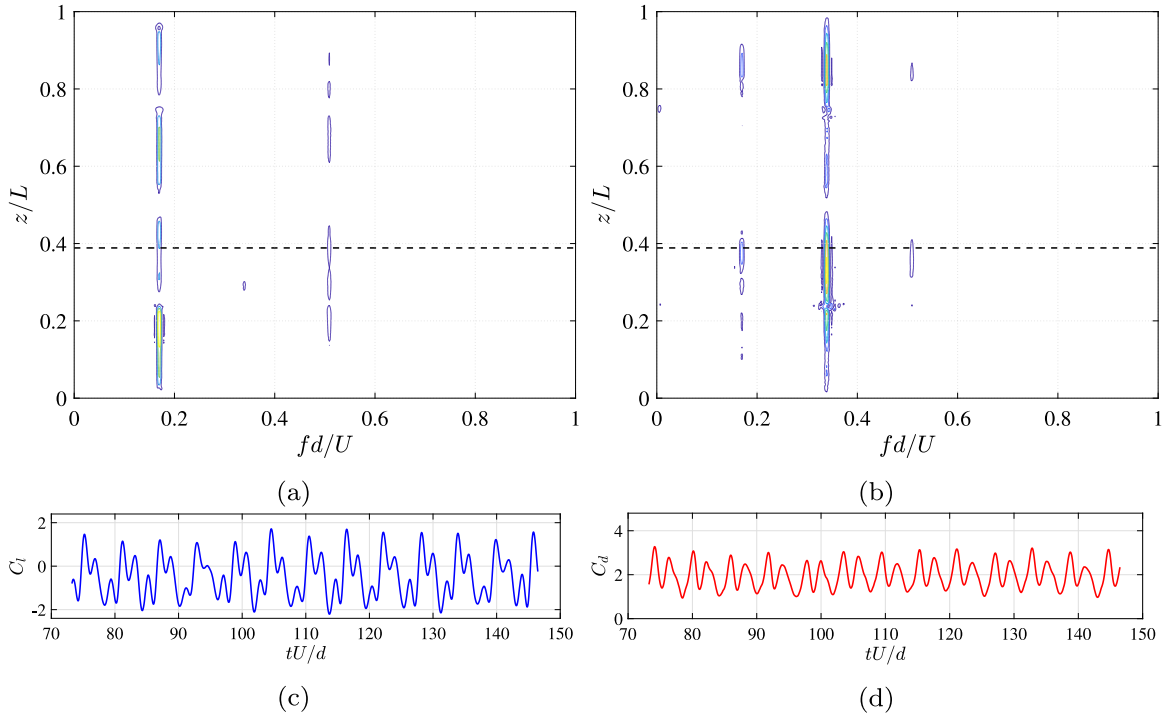


Fig. 4. Free vibration: Fluid force coefficients along the cylinder span of uniform current at $U_r = 12.66$: (a) C_l frequency response; (b) C_d frequency response; (c) and (d) C_l and C_d time traces at location $z/d = 0.395$, respectively (denoted by black dash line in (a) and (b)).

mass coefficient C_m (C_{my} in the CF direction and C_{mx} in the IL direction), can be obtained using the following equations,

$$C_v = \frac{\frac{2}{T_v} \int_{T_v} (\tilde{C}(t) \tilde{\xi}(t)) dt}{\sqrt{\frac{2}{T_v} \int_{T_v} (\tilde{\xi}^2(t)) dt}}, \quad (5)$$

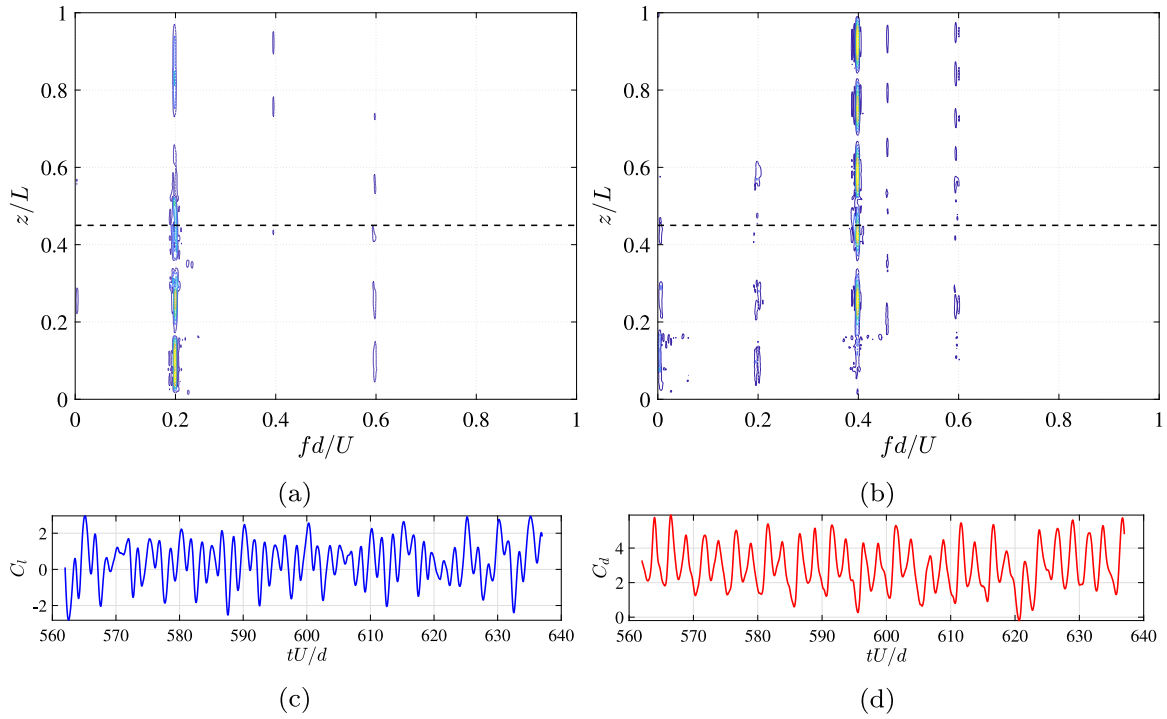


Fig. 5. Free vibration: Fluid force coefficients along the cylinder span subject to linearly sheared current at $U_r = 15.65$ with $U_{max} = 1.4U_\infty$ and $U_{min} = 0.6U_\infty$. See Fig. 4 for the caption of each subfigure.

$$C_m = -\frac{2U_\infty^2}{\pi D^2} \cdot \frac{\int_{T_v} (\tilde{C}(t) \tilde{\xi}(t)) dt}{\int_{T_v} (\tilde{\xi}^2(t)) dt}, \quad (6)$$

where $\tilde{\xi}$ is the oscillatory IL or the CF non-dimensional displacement response ($\tilde{\xi} = \xi - \bar{\xi}$), and $\dot{\tilde{\xi}}$ and $\ddot{\tilde{\xi}}$ are the first and second derivatives of ξ with respect to time, namely the IL or the CF non-dimensional velocity and acceleration. \tilde{C} is the sectional fluctuating drag or lift coefficients ($\tilde{C} = C - \bar{C}$) along the model span. T_v is the period of the cylinder vibration.

The values of above hydrodynamic coefficients obtained from the *free vibration* and *forced vibration* are plotted together in Fig. 6, where the top three subfigures show the amplitude response $\frac{A_x}{d}$, $\frac{A_y}{d}$ and phase response θ along the flexible model, while the subfigures of the second to fifth row plot the distributions of C_{lv} , C_{my} , C_{dv} and C_{mx} , respectively, where the solid line is the result of *free vibration* and the dots are results of *forced vibration*. In general, in both uniform (left and middle panels) and linearly sheared flow (right panel), we observe that for all the hydrodynamic coefficients, the *forced vibration* is in good agreement with the *free vibration*. Nonetheless, there are several points that deserve our attention. First of all, the simulation of *forced vibration* correctly predicts the variation of positive and negative C_{lv} , shown in Fig. 6(d), (e) and (f). The positive C_{lv} is mainly associated with a counter-clockwise (CCW) trajectory, which was first established in the rigid cylinder experiment by Dahl et al. (2006) and flexible cylinder simulations by Bourguet et al. (2011). Note that the CCW trajectory could be identified by $\theta \in [0, \pi]$, while the clockwise (CW) trajectory corresponds to $\theta \in [\pi, 2\pi]$, as shown in Fig. 6(a), (b) and (c). Secondly, in both *free vibration* and *forced vibration* simulations, the magnitude of (C_{dv}) varies less significantly along the cylinder span than that of C_{lv} , see Fig. 6(j), (k) and (l). Furthermore, similar to the *free vibration*, the simulation of *forced vibration* also correctly predicts the C_{my} variation. In contrast to C_{my} 's large variation along the span, all the cases show that C_{mx} remains relatively flat, see Fig. 6(m), (n) and (o).

So far we have shown that all the four hydrodynamic coefficients are similar between the *free vibration* and *forced vibration*. However to corroborate the strip theory, it is necessary to demonstrate that the near wake patterns also resemble each other, as the fluid flow and the structure response of a VIV problem are fully coupled. Here, the wake flow behind the flexible cylinder at $U_r = 12.66$ of uniform flow is visualized in Fig. 7(a), where the vortical structures are represented by iso-surfaces of $Q = 0.1$ and colored by ω_z . We observe that the vortices behind the cylinder are separated into different cells along the cylinder span. Specifically, the vortices along the span can be divided into four zones consisting of two patterns, one of which is the region of clear straight vortex tubes and the other one exhibits wavy vortex tubes with strong stream-wise vortices. In order to establish the connection of such spanwise vortical wake to the

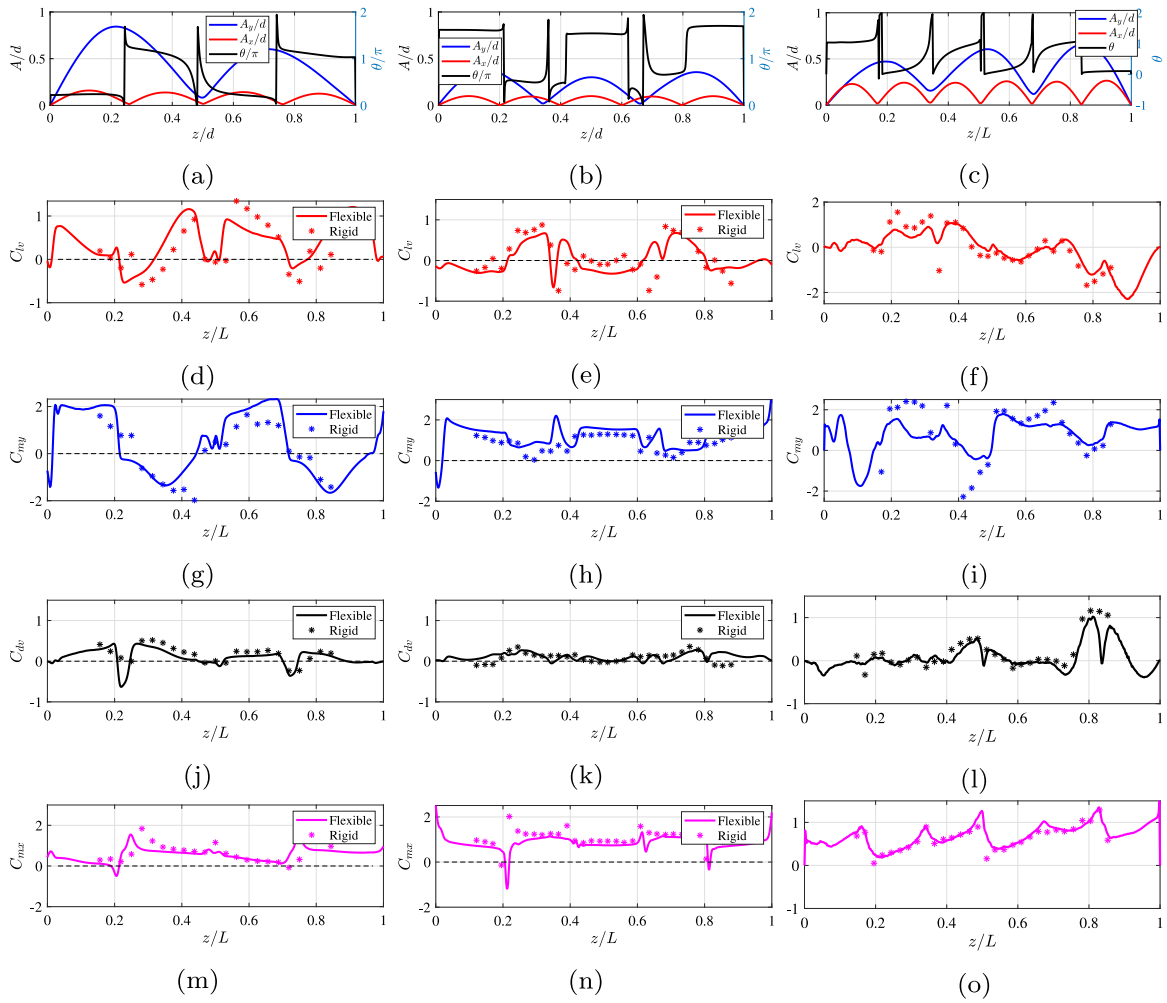


Fig. 6. Cylinder response and hydrodynamic coefficients distributions along the cylinder span at $U_r = 12.66$ of uniform flow (left panel), $U_r = 13.61$ of uniform flow (middle panel) and $U_r = 15.65$ of linearly sheared flow (right panel): (a), (b) and (c), IL and CF amplitude and phase θ responses; (d), (e) and (f), C_{lv} ; (g), (h) and (i), C_{my} ; (j), (k) and (l), C_{dv} ; (m), (n) and (o), C_{mx} . Solid line is from the simulation of *free vibration*, dot denotes the corresponding simulation results from the *forced vibration*.

hydrodynamic coefficients, the CF and IL amplitude, power spectral density (PSD) of the CF displacement, PSD and phase angle of the CF component of the flow velocity probed at three diameters downstream from the mean IL displacement are given in Fig. 7(b), (c), (d) and (e), respectively. Comparing the PSD of the structure vibration response in Fig. 7(c) with the PSD of CF component of the flow velocity in Fig. 7(d), we see that the “lock-in” happens in the entire model span, as the CF vibration frequency is equal to the vortex shedding frequency everywhere. However, the phase analysis of the flow velocity reveals that the relative phase angle of the CF component of the flow velocity keeps a relatively constant value in the half wavelength between two adjacent IL nodes, and changes drastically at IL nodes. As a result, over that half wavelength of the IL mode, the vortical structures develop into similar patterns and at the IL nodes, across which the IL motion changes by 180° in phase angle. In summary, for a flexible cylinder in uniform flow, vortices will shed in cells along the model cylinder span with the cells separated by the IL nodes. The relative motion between the local cylinder and the vortex formation is affected by the cell structure, which gives rise to the discontinuous distribution of the added mass along the flexible cylinder span.

The vortices behind the flexible cylinder in linearly sheared flow are also separated into different cells along the cylinder span, which is visualized in Fig. 8(a), where the vortical structures are represented by iso-surfaces of $Q = 0.1$ and colored by ω_z . However, different from the case of uniform flow, here we can observe strong spanwise vortex shedding accompanied denser streamwise vortices where inflow velocity is higher. The CF and IL amplitude, power spectral density (PSD) of the CF displacement, PSD and phase angle of the CF component of the flow velocity probed at three diameters downstream from the mean IL displacement are given in Fig. 8(b), (c), (d) and (e), respectively. Comparing the PSD of the structure vibration response in Fig. 8(c) with the PSD of CF component of the flow velocity in Fig. 8(d), it can be seen that

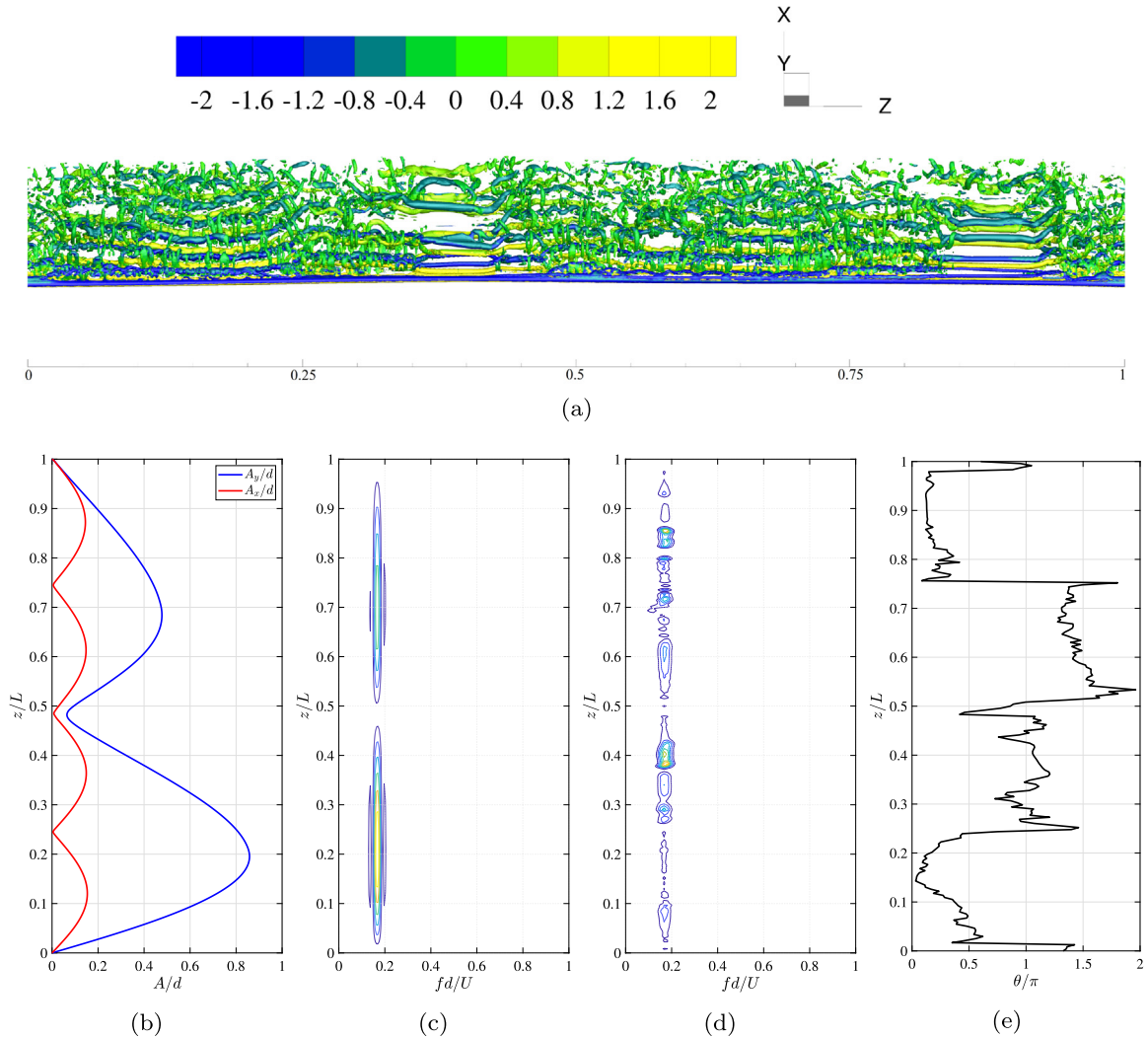


Fig. 7. Free vibration in uniform flow: connection between the wake pattern and the hydrodynamic coefficients at $U_r = 12.66$. (a) vortices behind the flexible cylinder; (b) amplitude response; (c) PSD of CF displacement; (d) PSD of CF component of the flow velocity; (e) relative phase angle of the CF component of the flow velocity that is probed at three diameters downstream from the mean IL displacement. Note that the vortices are visualized by iso-surfaces of $Q = 0.1$ and colored by the magnitude of ω_z . (For interpretation of the references to color in this figure legend, the reader is referred to the web version of this article.)

the “lock-in” does not happen in the entire span section, as the CF vibration frequency is not equal to the vortex shedding frequency in lower inflow velocity region. Furthermore, the phase analysis of the flow velocity reveals that the relative phase angle of the CF component of the flow velocity keeps a relatively constant value in the half wavelength between two adjacent IL nodes. In addition, compared to the uniform flow case, we see the phase shift in span direction indicating an oblique vortex shedding subject to linearly sheared flow.

Keeping the vortex cells of the *free vibration* in mind, let us examine the simulation results of *forced vibration*. On one hand, for the *free vibration* at $U_r = 12.66$, the near wake vorticity field as well as the sectional hydrodynamic force at location $z/L = 0.127$ and $z/L = 0.314$ are shown in Figs. 9 and 11, respectively. Specifically, subfigures (a)–(d) show four consecutive 2D snapshots of the ω_z field over one period of the CF vibration, subfigure (e) plots the time trace of the cylinder motions, and subfigure (f) exhibits the time trace of the lift coefficient. On the other hand, the simulation results of the corresponding *forced vibration* are plotted in Figs. 10 and 12. At location $z/L = 0.127$, the local wake pattern of the *free vibration* and *forced vibration* are both classical “2S” mode, and the fluctuating lift force is in anti-phase with acceleration.

At spanwise location $z/L = 0.314$, a similarity can also be found in the fluctuating lift force in phase with acceleration, see Fig. 11(f) and Fig. 12(f). However, the vortex formation of the *free vibration* is slightly different from that of the *forced vibration*; the former displays “P+S” mode while the later shows a symmetric “2P” mode, as shown in Fig. 11(a)–(d)

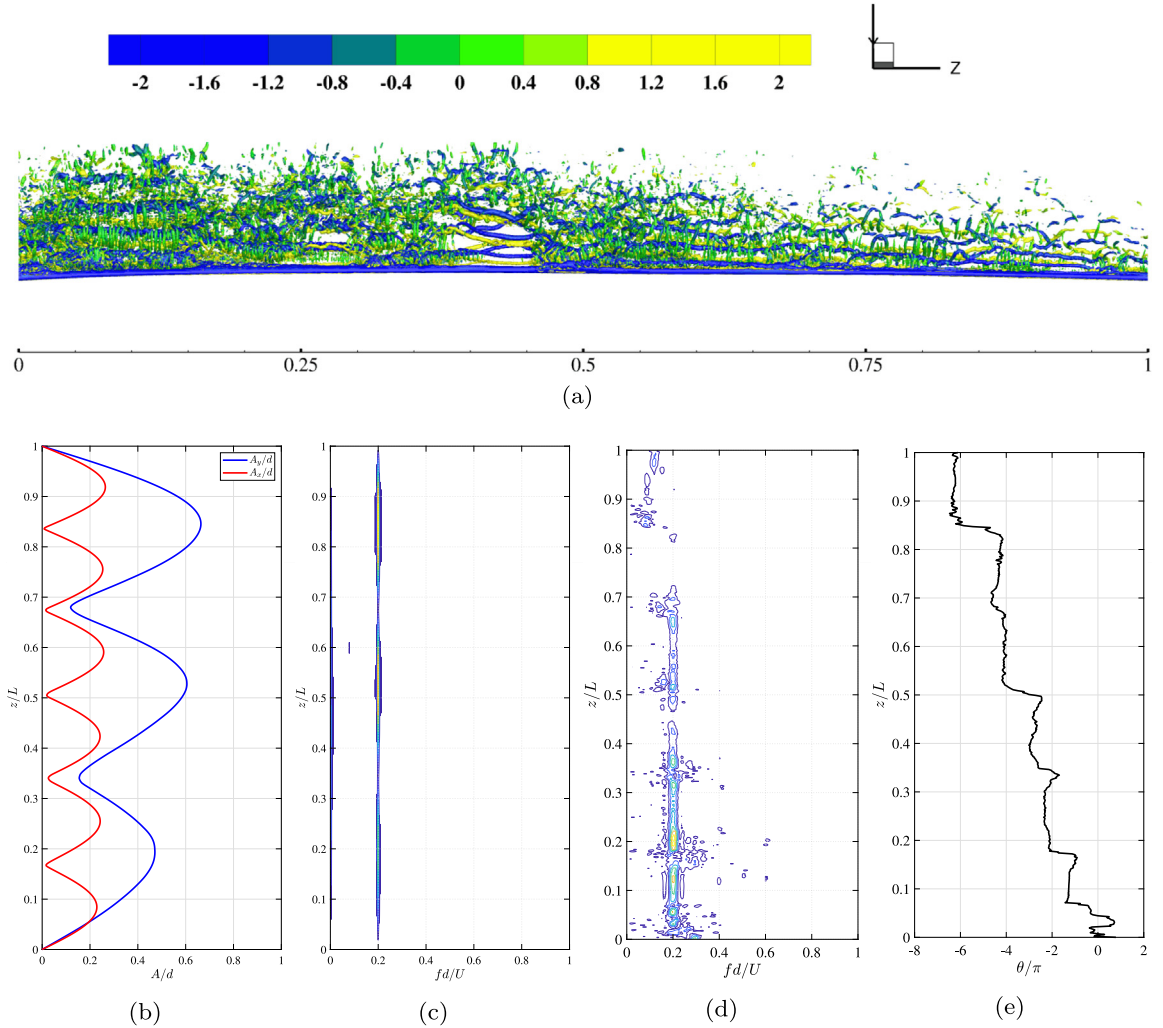


Fig. 8. Free vibration in linearly sheared flow: connection between the wake pattern and the hydrodynamic coefficients at $U_r = 15.65$ ($U_{max} = 1.4U_\infty$, $U_{min} = 0.6U_\infty$). (a) vortices behind the flexible cylinder; (b) amplitude response; (c) PSD of CF displacement; (d) PSD of CF component of the flow velocity; (e) relative phase angle of the CF component of the flow velocity that is probed at three diameters downstream from the mean IL displacement. Note that the vortices are visualized by iso-surfaces of $Q = 0.1$ and colored by the magnitude of ω_z . (For interpretation of the references to color in this figure legend, the reader is referred to the web version of this article.)

and Fig. 12(a)–(d), respectively. The pattern difference is due to the difference of the motion, as for the *forced vibration* strictly sinusoidal motions are imposed, while for the *free vibration*, non-sinusoidal motions with non-zero equilibrium and slightly varying amplitude are observed, see Fig. 12(e) and Fig. 11(e), respectively. In addition, comparing with the distribution of C_{my} along the cylinder shown in Fig. 6(e), we can conclude that the vortex shedding pattern is strongly related to the sign of C_{my} , e.g., at $z/L = 0.314$, $C_{my} < 0$ is associated with the “P+S” mode, and at $z/L = 0.127$, $C_{my} > 0$ is associated with the “2S” mode.

The near wake vorticity field and the sectional hydrodynamic force at locations $z/L = 0.22$ and $z/L = 0.46$ of the *free vibration* in linearly sheared flow, and the corresponding counterparts of *forced vibration* are shown in Fig. 13, Fig. 14, Fig. 15 and Fig. 16, respectively. Once again, similarities in terms of vortex shedding pattern and the value of hydrodynamic coefficients could be observed between the *free vibration* and the corresponding *forced vibration*, although strong traveling waves exist in this case. In addition, the correlation between the vortex mode “2P” or “P+S” and the negative value of C_{my} can be found in the linearly sheared flow case as well.

4. Summary

We performed large-eddy simulations of the free vibration of a long uniform flexible cylinder (*free vibration*) both in uniform and linearly sheared flow and corresponding *two-dimensional* simulations of a forced vibrating rigid cylinder

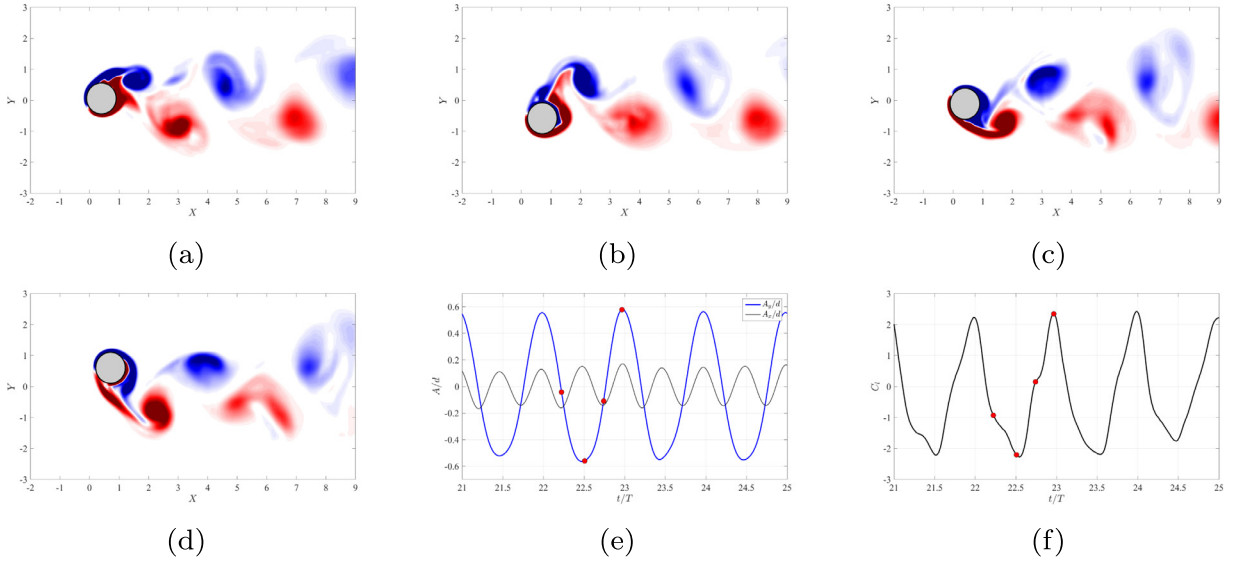


Fig. 9. Free vibration at $z/d = 0.127$, $U_r = 12.66$ ($C_{my} = 1.91$): (a)–(d) two-dimensional slices of the instantaneous field of ω_z ; (e) time trace of the cylinder motions; (f) oscillating lift force. The blue line in subfigure (e) corresponds to the CF displacement, and the black line denotes the IL displacement. The red circle highlights the corresponding time of the snapshots in subfigure (a)–(e).

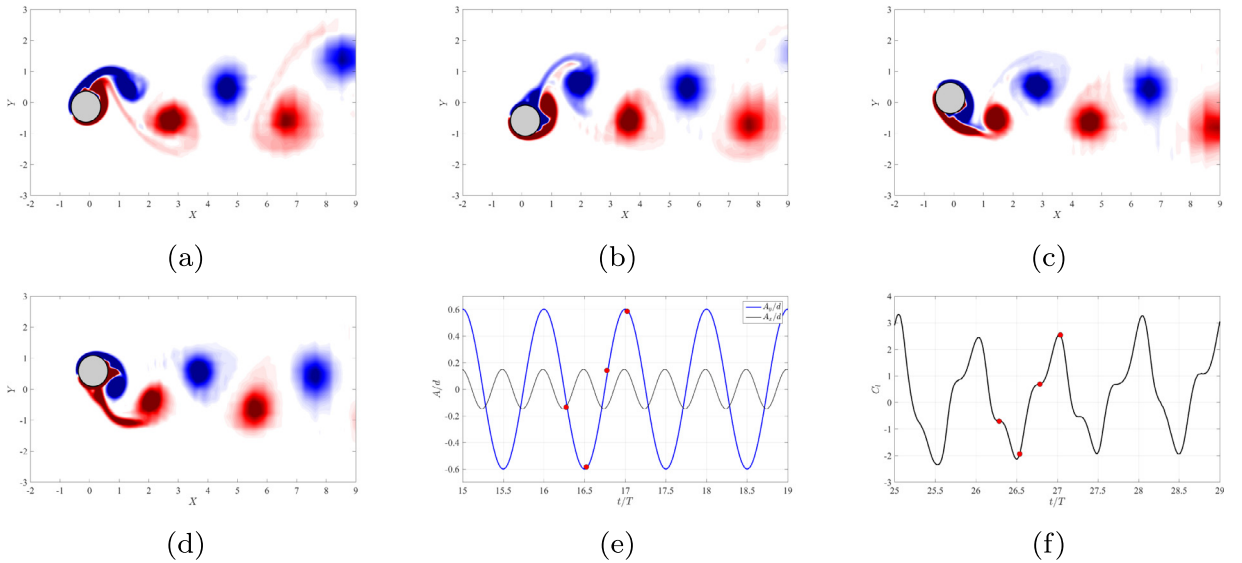


Fig. 10. Forced vibration at $U_r = 12.66$ ($C_{my} = 1.56$): vorticity field, cylinder motions and lift force. Note that here the cylinder motions are prescribed by Eq. (4), where the value of the amplitude and frequency are taken from the *free vibration* shown in Fig. 9. See Fig. 9 for the caption of each subfigure.

(forced vibration). By comparing the simulation results of *free vibration* with those of *forced vibration*, we observed that the hydrodynamic coefficients are in good agreement between the two cases. Along the span, at the same vibrating amplitude and frequency, the *forced vibration* resembles closely the classical “2S” vortex shedding mode of the *free vibration*, but the *forced vibration* gives rises to a symmetric “2P” pattern when the *free vibration* shows a slightly different pattern,

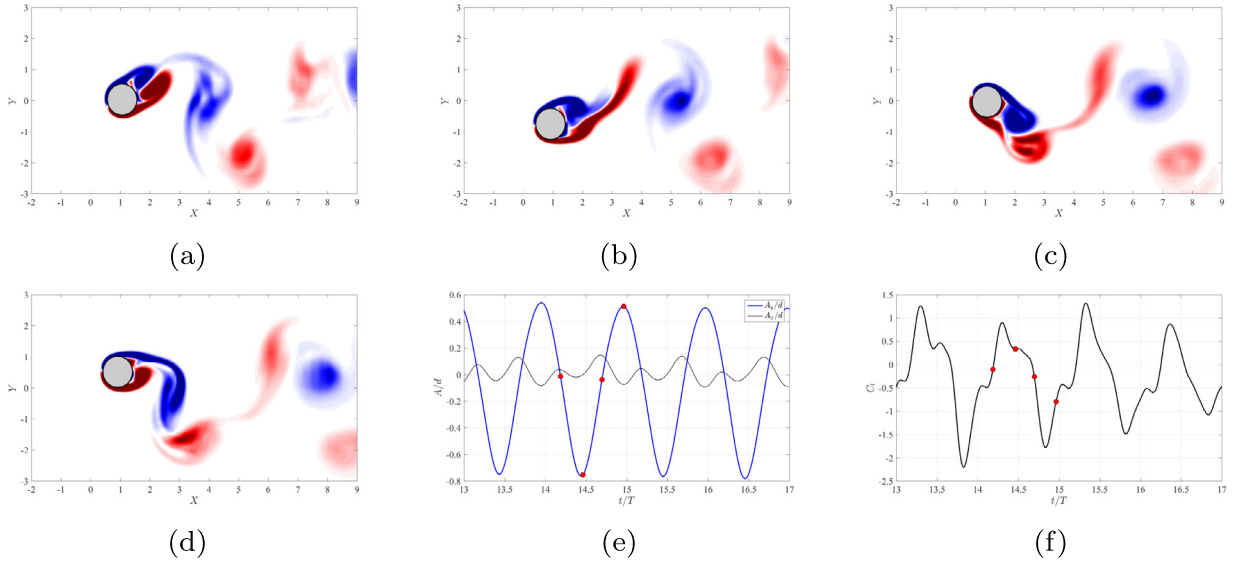


Fig. 11. Free vibration at $U_r = 12.66$, $z/d = 0.314$ ($C_{my} = -1.02$): two-dimensional vorticity snapshots, cylinder motions and lift force. See Fig. 9 for the caption of each subfigure.

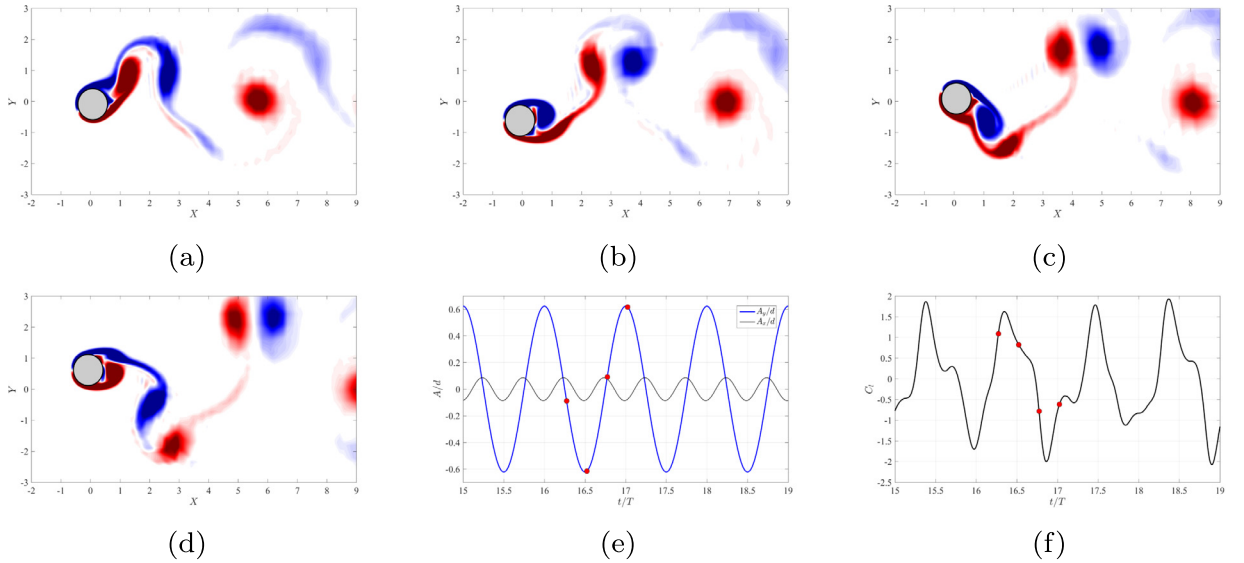


Fig. 12. Forced vibration at $U_r = 12.66$ ($C_{my} = -0.96$): vorticity snapshots, cylinder motions and lift force. See Fig. 9 for the caption of each subfigure. Note that here the cylinder motions are prescribed by Eq. (4), where the value of the amplitude and frequency is taken from the *free vibration* shown in Fig. 11.

namely “P+S”. Moreover, both *forced vibration* and *free vibration* confirm the previous finding that the positive C_{lv} is mainly associated with a counter-clockwise (CCW) trajectory. They also reveal the fact that a positive value of the added mass in the CF direction (C_{my}) is associated with the “2S” mode while a negative value of C_{my} is always associated with the “P+S” or “2P” mode.

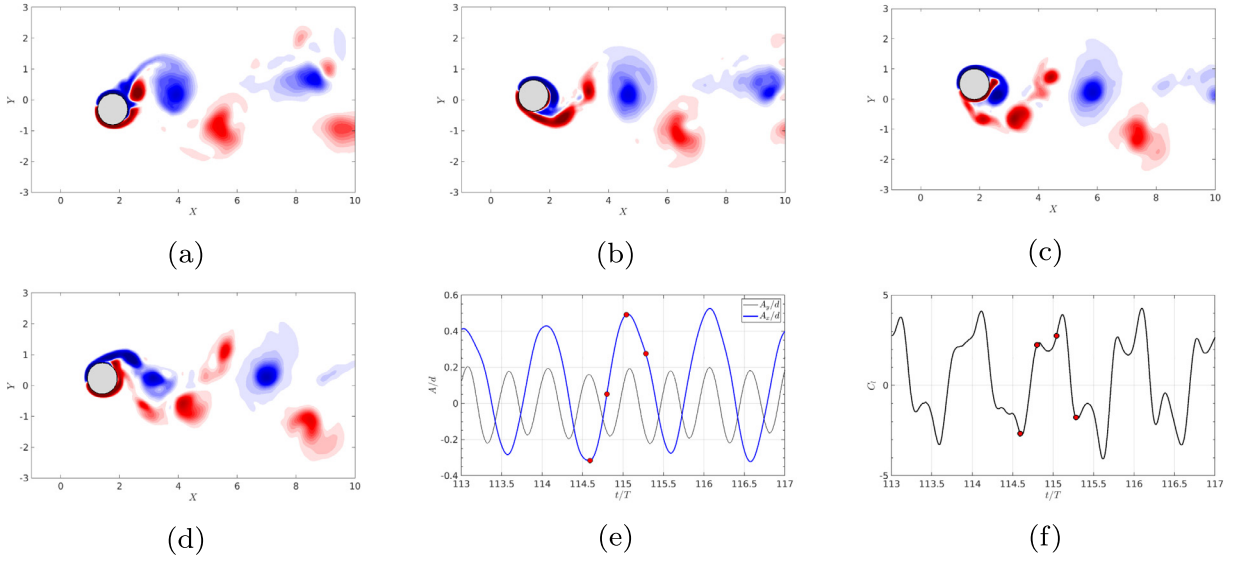


Fig. 13. Free vibration in linearly sheared current at $U_r = 15.65$ ($U_{max} = 1.4U_\infty$, $U_{min} = 0.6U_\infty$, $C_{my} = 1.55$), $z/d = 0.22$. See Fig. 9 for the caption of each subfigure.

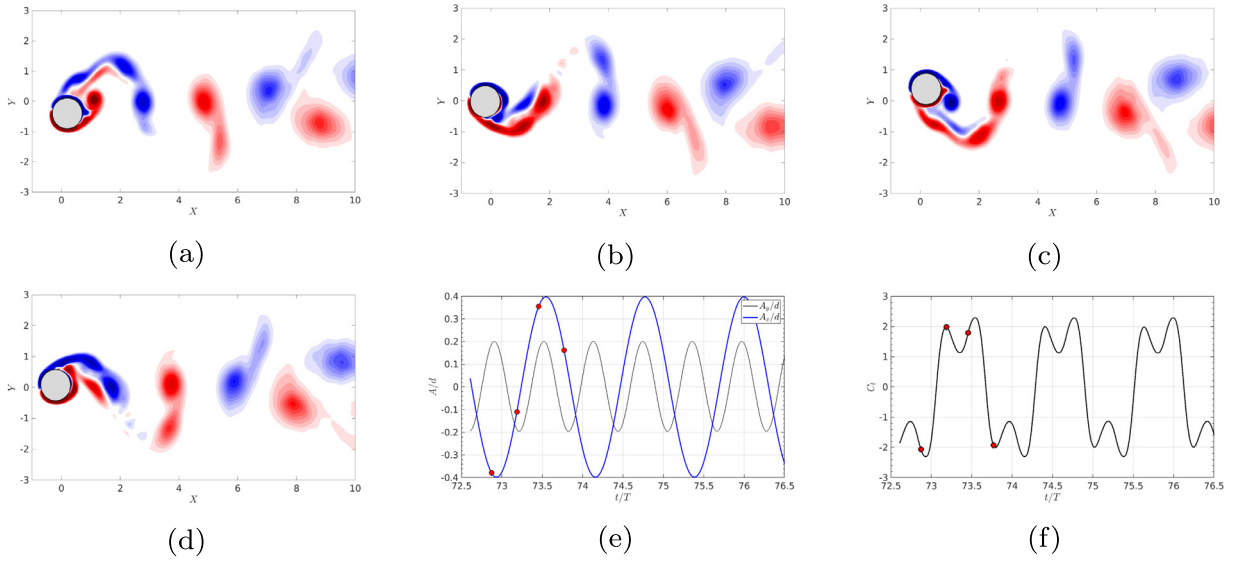


Fig. 14. Forced vibration in linearly sheared current at $U_r = 15.65$ ($C_{my} = 2.06$). See Fig. 9 for the caption of each subfigure. Note that here the cylinder motions are prescribed by Eq. (4), where the value of the amplitude and frequency is taken from the free vibration shown in Fig. 13.

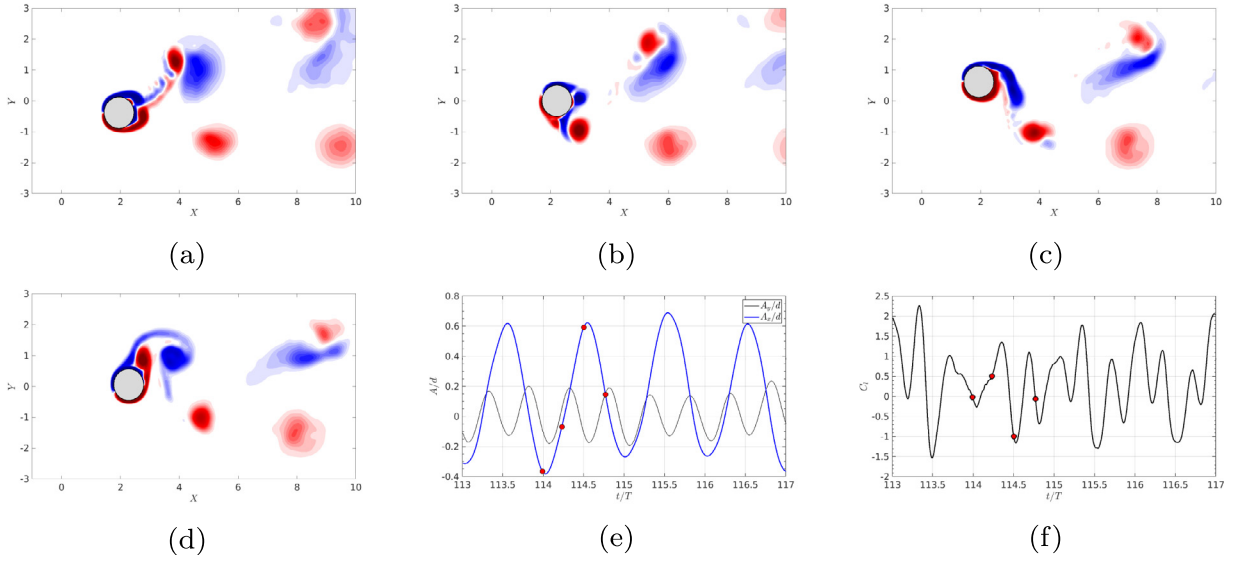


Fig. 15. Free vibration in linearly sheared current at $U_r = 15.65$ ($U_{max} = 1.4U_\infty$, $U_{min} = 0.6U_\infty$, $C_{my} = -0.37$), $z/d = 0.46$. See Fig. 9 for the caption of each subfigure.

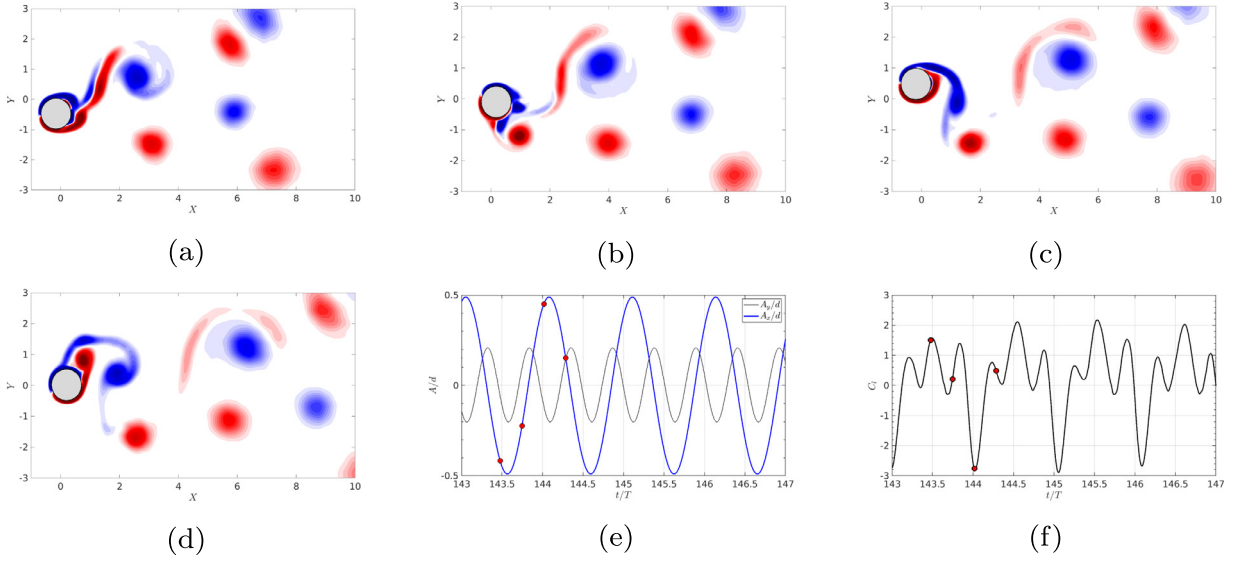


Fig. 16. Forced vibration in linearly sheared current at $U_r = 15.65$ ($C_{my} = -1.06$). See Fig. 9 for the caption of each subfigure. Note that here the cylinder motions are prescribed by Eq. (4), where the value of the amplitude and frequency is taken from the free vibration shown in Fig. 15.

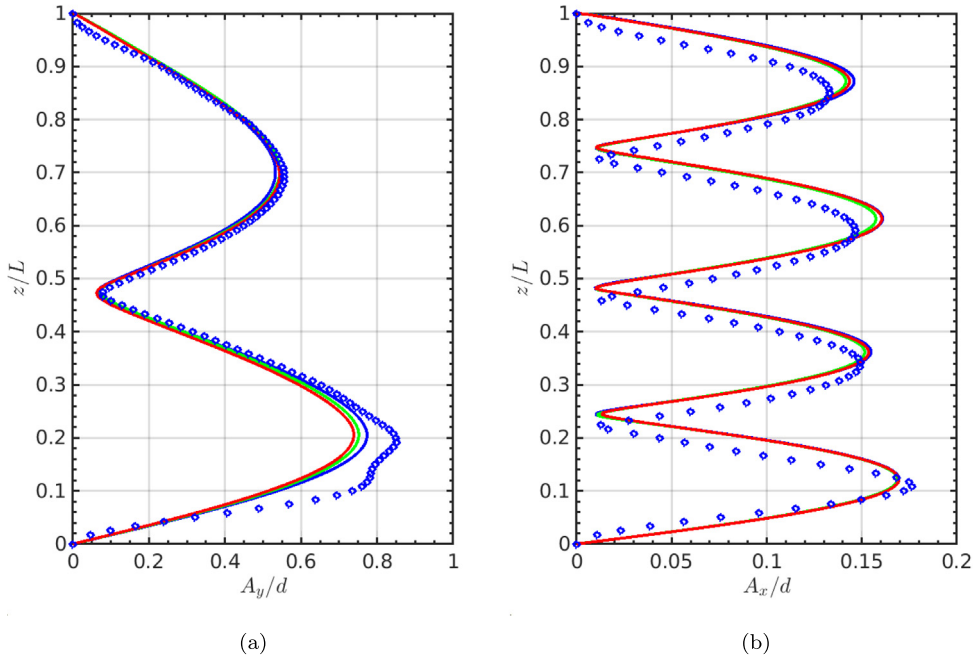


Fig. A.17. Comparison between the simulation results of different resolutions and experiment measurement of A_y/d and A_x/d along the cylinder span at $Re = 650$ and $U_r = 12.66$ (modal group “4/2”): blue symbols, experimental measurement; red lines, 512 Fourier planes; green lines, 640 Fourier planes; blue lines, 768 Fourier planes. (For interpretation of the references to color in this figure legend, the reader is referred to the web version of this article.)

CRediT authorship contribution statement

Zhicheng Wang: Conceptualization, Methodology, Data analysis, Writing. **Dixia Fan:** Data analysis, Writing. **Michael S. Triantafyllou:** Supervision, Funding acquisition, Writing. **George Em Karniadakis:** Supervision, Funding acquisition, Writing.

Declaration of competing interest

The authors declare that they have no known competing financial interests or personal relationships that could have appeared to influence the work reported in this paper.

Acknowledgments

The authors acknowledge with gratitude support from Chevron Energy Technology Company and BP Exploration Operating Company Limited. All computations were performed at Center for Computation & Visualization, Brown University.

Appendix A. Mesh independence study

In order to demonstrate that the mesh resolution of 512 Fourier planes along the cylinder span is adequate for current LES, for the case of $U_r = 12.66$ ($Re = 650$) in uniform flow, we performed two additional simulations, one uses 640 Fourier planes, the other one uses 768 Fourier planes. Note that, the two additional simulations start from the simulation result of 512 Fourier planes, and the computational time $250tU_\infty/d = 250$. The amplitude response in both the CF and IL direction are plotted in Fig. A.17. We see a good agreement between the simulation and experiment. Both the simulation and experiment show that the flexible cylinder vibrates at modal group “4/2”. We can also observe that the change of the simulation result is negligible as the resolution is increased from 512 to 768 Fourier planes.

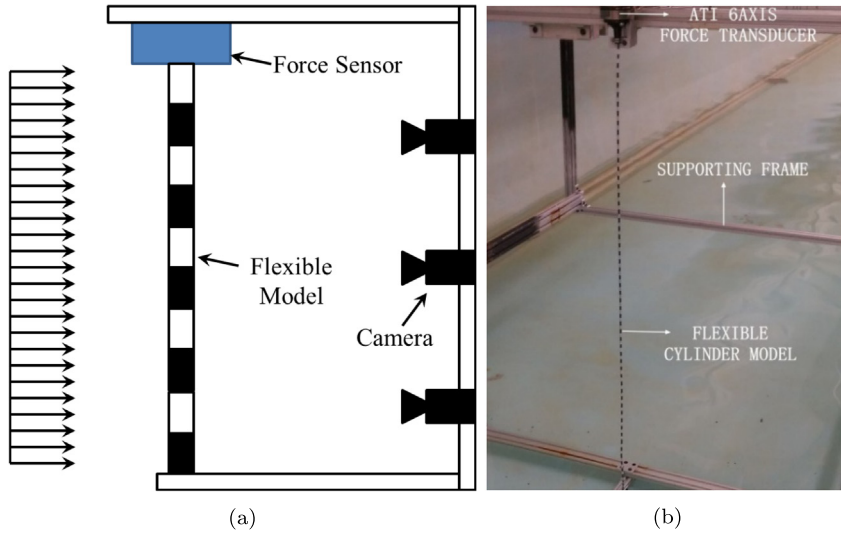


Fig. B.18. The flexible model in the MIT Towing Tank: (a) a sketch of the experimental setup that shows the uniform incoming flow and the black and white strips used for motion tracking purposes; (b) an actual photo of the flexible model setup with the support frame.

Appendix B. Experimental validation of the large-eddy simulation results

Here, we validate the LES results by the corresponding experimental measurements on the frequency and displacement response of the flexible cylinder. In the experiment, we keep the same dimensionless parameters as in the simulation, in terms of the Reynolds number, mass ratio and aspect ratio. Moreover, in order to mimic the linear tension along the cylinder in the experiment, the dimensionless tension T in Eq. (2) varies at the same rate as that of the experiment. The motion of the cylinder in the experiment is recorded by the underwater optical measurement system described in detail in Fan et al. (2016). Fig. B.18 shows a sketch (a) and a photo of the experimental setup of the flexible model in the MIT Towing Tank Lab.

From $U_r = 10.75$ to $U_r = 17.22$, the maximum of the 1/10th highest peak of the CF and IL amplitude response along the model span as well as the non-dimensional frequency response in the CF direction are plotted in Fig. B.19, where the experimental measurements are denoted by blue dots and the simulation results are denoted by red circles. We see that the simulation results agree with those of the experiment very well, as the flexible cylinder switches from the modal group “4/2” to the modal group “6/3”, when U_r increases from 10.75 to 17.22. In addition, both the experiment and the simulation results reveal that the maximum amplitude of the uniform flexible cylinder in both the IL and the CF direction monotonically increases with U_r in the same modal group, while the non-dimensional frequency stays at a relatively constant value inside the same modal group. Both the amplitude and frequency responses jump significantly when the modal group changes.

The comparison of the C_{lv} , C_{dv} , C_{my} and C_{mx} along the model span between the experiment and simulation is presented in Fig. B.20(a), Fig. B.20(b), Fig. B.20(c) and Fig. B.20(d), respectively. For all the four hydrodynamic coefficients, the simulation results agree with those of the experiment very well. Note that the fluid forces along the model span in the experiment are reconstructed from the measured motion via the inverse force reconstruction method; see details in Fan (2019).

Appendix C. Additional simulation case on the flexible cylinder in linearly sheared flow

In this section, the main simulation result of the *free vibration* in linearly sheared current of $U_r = 15.65$ with $U_{max} = 1.375U_\infty$, $U_{min} = 0.625U_\infty$ is presented. In Fig. C.21(c), it can be seen that the flexible cylinder vibrates at the 6th mode in the IL direction and at the 3rd mode in the CF direction. However, different from the sheared flow case shown in Fig. 3, here standing wave response is observed in the CF direction. Nonetheless, the simulation results of the *forced vibration* agree with corresponding *flexible vibration* very well, see Fig. C.22(b) of C_{lv} , Fig. C.22(c) of C_{my} , Fig. C.22(d) of C_{dv} and Fig. C.22(b) of C_{mx} .

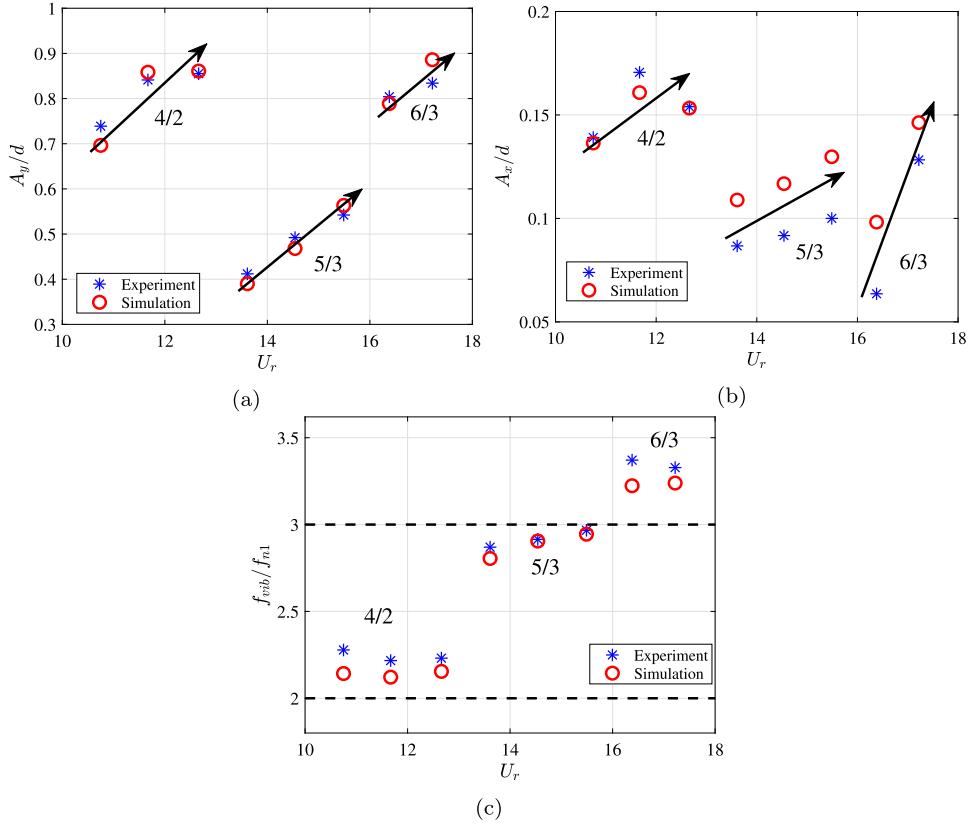


Fig. B.19. Comparison between the simulation and the experiment from $U_r = 10.75$ to $U_r = 17.22$: (a) maximum of CF displacement response; (b) maximum of CF displacement response; (c) non-dimensional frequency response in the CF direction. Note red circles denote simulation results, blue symbols are experimental measurements. The black arrows indicate the trend of the variation of the amplitude in a same modal group. The dashed horizontal line denotes n th times model natural frequency in still water. (For interpretation of the references to color in this figure legend, the reader is referred to the web version of this article.)

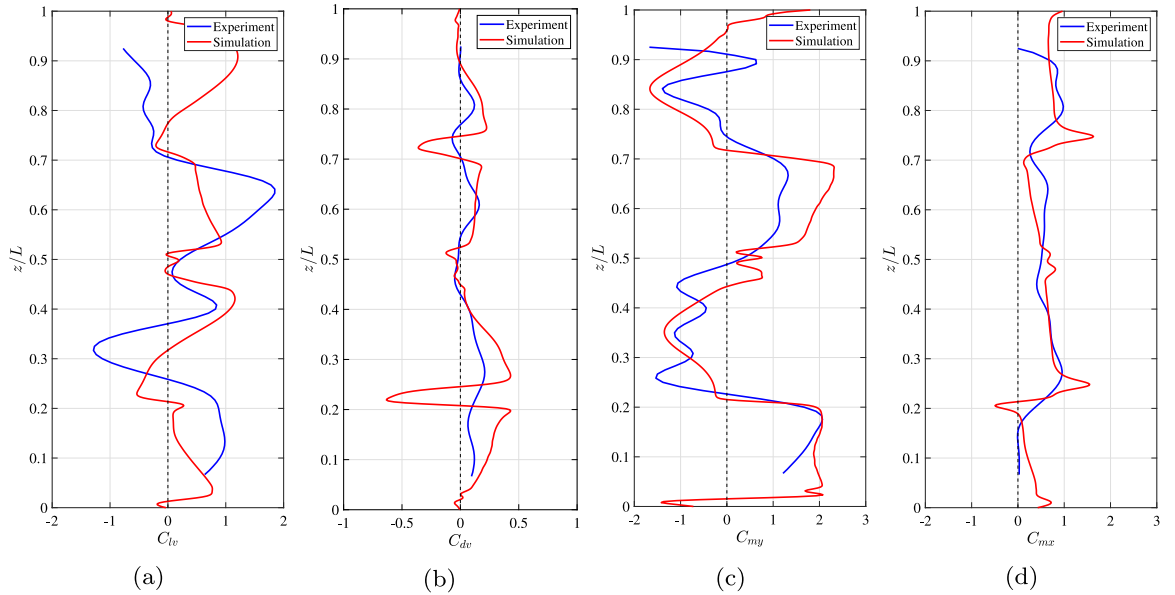


Fig. B.20. Comparison between the simulation (red line) and the experiment (blue line) at $U_r = 12.66$ (modal group "4/2") along the cylinder span: (a) C_{lv} ; (b) C_{dv} ; (c) C_{my} ; (d) C_{mx} . (For interpretation of the references to color in this figure legend, the reader is referred to the web version of this article.)

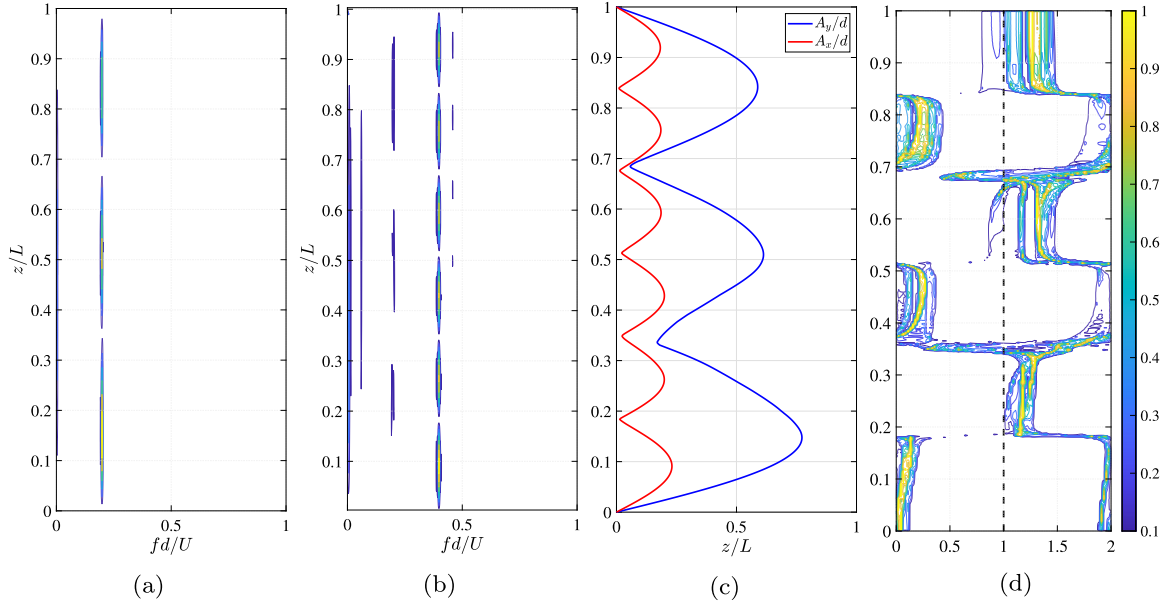


Fig. C.21. Free vibration in linear shear current at $U_r = 15.65$ with $U_{max} = 1.375U_\infty$ and $U_{min} = 0.625U_\infty$. See Fig. 1 for the caption of each subfigure.

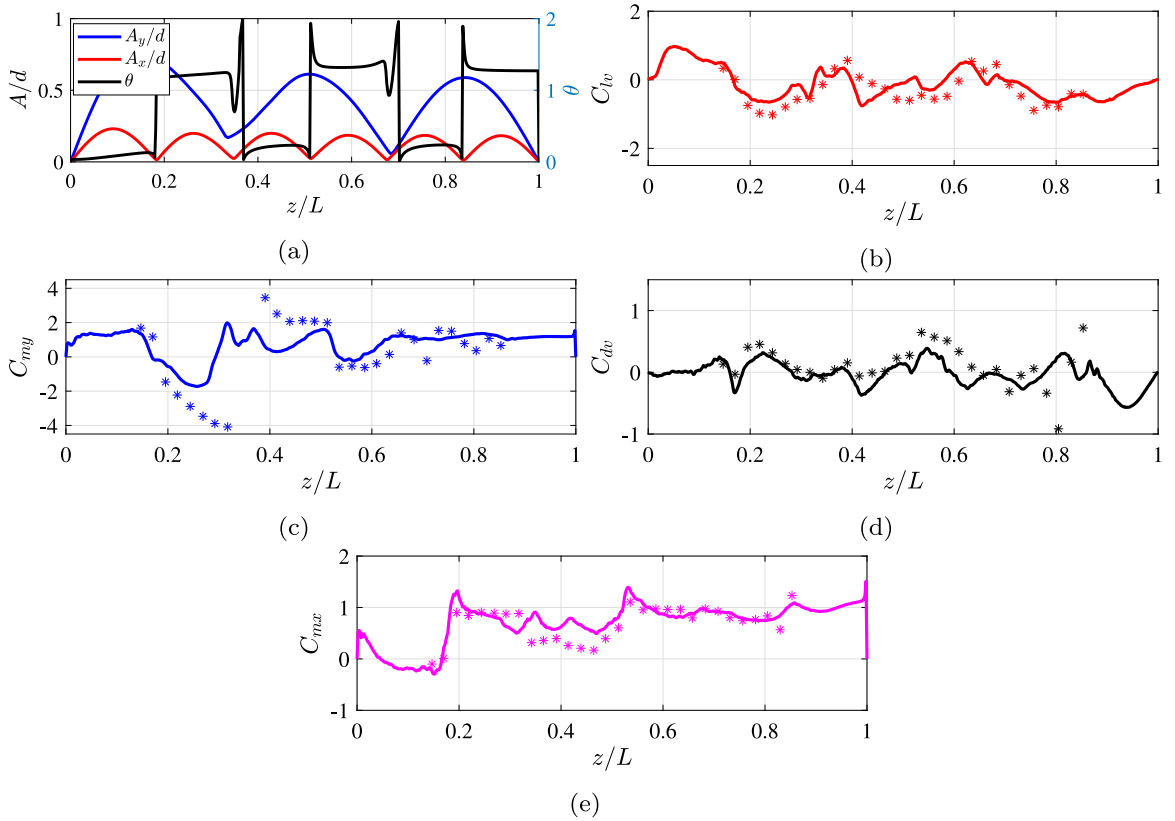


Fig. C.22. Cylinder response and hydrodynamic coefficients distributions along the cylinder span in linear shear current at $U_r = 15.65$ with $U_{max} = 1.375U_\infty$ and $U_{min} = 0.625U_\infty$: (a) IL and CF amplitude and phase θ responses; (b) C_{lw} ; (c) C_{my} ; (d) C_{dw} ; (e) C_{mx} . Solid line is from the simulation of free vibration, dot denotes the corresponding simulation results from the forced vibration.

References

- Blackburn, H., Govardhan, R.N., Williamson, C.H.K., 2000. A complementary numerical and physical investigation of the vortex-induced vibration. *J. Fluids Struct.* 15 (481–488).
- Bourguet, R., Karniadakis, G.E., Triantafyllou, M.S., 2013a. Multi-frequency vortex-induced vibrations of a long tensioned beam in linear and exponential shear flows. *J. Fluids Struct.* 41, 33–42.
- Bourguet, R., Karniadakis, G.E., Triantafyllou, M.S., 2013b. Phasing mechanisms between the in-line and cross-flow vortex-induced vibrations of a long tensioned beam in shear flow. *Comput. Struct.* 122, 155–163.
- Bourguet, R., Modarres-Sadeghi, Y., Karniadakis, G.E., Triantafyllou, M.S., 2011. Wake-body resonance of long flexible structures is dominated by counterclockwise orbits. *Phys. Rev. Lett.* 107 (13), 134502.
- Carberry, J., Sheridan, J., Rockwell, D., 2003. Controlled oscillations of a cylinder: a new wake state. *J. Fluids Struct.* 17 (2), 337–343.
- Carberry, J., Sheridan, J., Rockwell, D., 2005. Controlled oscillations of a cylinder: forces and wake modes. *J. Fluid Mech.* 538, 31–69.
- Dahl, J.M., 2008. Vortex-induced vibration of a circular cylinder with combined in-line and cross-flow motion (Ph.D thesis). Massachusetts Institute of Technology.
- Dahl, J.M., Hover, F.S., Triantafyllou, M.S., 2006. Two-degree-of-freedom vortex-induced vibrations using a force assisted apparatus. *J. Fluids Struct.* 22 (6), 807–818.
- Dahl, J.M., Hover, F.S., Triantafyllou, M.S., Dong, S., Karniadakis, G.E., 2007. Resonant vibrations of bluff bodies cause multivortex shedding and high frequency forces. *Phys. Rev. Lett.* 99 (14), 144503.
- Dahl, J.M., Hover, F.S., Triantafyllou, M.S., Oakley, O., 2010. Dual resonance in vortex-induced vibrations at subcritical and supercritical Reynolds numbers. *J. Fluid Mech.* 643, 395–424.
- Evangelinos, C., Karniadakis, G.E., 1999. Dynamics and flow structures in the turbulent wake of rigid and flexible cylinders subject to vortex-induced vibrations. *J. Fluid Mech.* 400, 91–124.
- Evangelinos, C., Lucor, D., Karniadakis, G.E., 2000. DNS-derived force distribution on flexible cylinders subject to vortex-induced vibration. *J. Fluids Struct.* 14 (3), 429–440.
- Fan, D., 2019. Mapping the hydrodynamic properties of flexible and rigid bodies undergoing vortex-induced vibrations (Ph.D thesis). Massachusetts Institute of Technology.
- Fan, D., Du, H., Triantafyllou, M.S., 2016. Optical tracking measurement on vortex induced vibration of flexible riser with short-length buoyance module. In: APS Division of Fluid Dynamics Meeting Abstracts.
- Fan, D., Triantafyllou, M.S., et al., 2017. Vortex induced vibration of riser with low span to diameter ratio buoyancy modules. In: The 27th International Ocean and Polar Engineering Conference. International Society of Offshore and Polar Engineers.
- Fan, D., Wang, Z., Triantafyllou, M.S., Karniadakis, G.E., 2019. Mapping the properties of the vortex-induced vibrations of flexible cylinders in uniform oncoming flow. *J. Fluid Mech.* 881, 815–858.
- Gabbai, R., Benaroya, H., 2005. An overview of modeling and experiments of vortex-induced vibration of circular cylinders. *J. Sound Vib.* 282 (3–5), 575–616.
- Gopalkrishnan, R., 1993. Vortex-induced forces on oscillating bluff cylinders (Ph.D thesis). Massachusetts Institute of Technology.
- Govardhan, R.N., Williamson, C.H.K., 2000. Modes of vortex formation and frequency response of a freely vibrating cylinder. *J. Fluid Mech.* 420, 85–130.
- Guermond, J.-L., Pasquetti, R., Popov, B., 2011a. Entropy viscosity method for nonlinear conservation law. *J. Comput. Phys.* 230 (11), 4248–4267.
- Guermond, J.-L., Pasquetti, R., Popov, B., 2011b. From suitable weak solutions to entropy viscosity. *J. Sci. Comput.* 49 (1), 35–50.
- Han, Q., Ma, Y., Xu, W., Fan, D., Wang, E., 2018. Hydrodynamic characteristics of an inclined slender flexible cylinder subjected to vortex-induced vibration. *Int. J. Mech. Sci.* 148, 352–365.
- Huarte, F.J.H., Bearman, P.W., Chaplin, J.R., 2006. On the force distribution along the axis of a flexible circular cylinder undergoing multi-mode vortex-induced vibrations. *J. Fluids Struct.* 22 (6), 897–903.
- Karniadakis, G.E., Sherwin, S., 2005. *Spectral/hp Element Methods for Computational Fluid Dynamics*, 2nd ed. Oxford University Press, Oxford, UK.
- Larsen, C.M., Vikestad, K., Yttervik, R., Passano, E., Baarholm, G.S., 2001. *VIVANA Theory Manual*. Marintek, Trondheim, Norway.
- Newman, J.N., 2018. *Marine Hydrodynamics*. MIT Press.
- Newman, D., Karniadakis, G.E., 1996. Simulations of flow over a flexible cable: a comparison of forced and flow-induced vibration. *J. Fluids Struct.* 10 (5), 439–453.
- Newman, D., Karniadakis, G.E., 1997. A direct numerical simulation study of flow past a freely vibrating cable. *J. Fluid Mech.* 344, 95–136.
- Sarpkaya, T., 1978. Fluid forces on oscillating cylinders. NASA STI/Recon Technical Report A 78, pp. 275–290.
- Tang, G., Lu, L., Teng, B., Park, H., Song, J., Zhang, J., 2011. Identification of hydrodynamic coefficients from experiment of vortex-induced vibration of slender riser model. *Sci. China Technol. Sci.* 54 (7), 1894–1905.
- Triantafyllou, M.S., Triantafyllou, G., Tein, Y., Ambrose, B.D., et al., 1999. Pragmatic riser VIV analysis. In: Offshore Technology Conference. Offshore Technology Conference.
- Vandiver, J., 1999. *SHEAR7 Program User Manual*. Massachusetts Institute of Technology, Cambridge, MA.
- Wang, X., So, R., Chan, K., 2003. A non-linear fluid force model for vortex-induced vibration of an elastic cylinder. *J. Sound Vib.* 260 (2), 287–305.
- Wang, Z., Triantafyllou, M.S., Constantinides, Y., Karniadakis, G.E., 2018. A spectral-element/fourier smoothed profile method for large-eddy simulations of complex VIV problems. *Comput. Fluids*, 172, 84–96.
- Wang, Z., Triantafyllou, M.S., Constantinides, Y., Karniadakis, G.E., 2019. An entropy-viscosity large eddy simulation study of turbulent flow in a flexible pipe. *J. Fluid Mech.* 859, 691–730.
- Wu, J., 2011. Hydrodynamic force identification from stochastic vortex induced vibration experiments with slender beams. Norges teknisk-naturvitenskapelige universitet, Fakultet for ingeniørvitenskap og teknologi, Institutt for marin teknikk.
- Wu, X., Ge, F., Hong, Y., 2012. A review of recent studies on vortex-induced vibrations of long slender cylinders. *J. Fluids Struct.* 28, 292–308.
- Zheng, H., Dahl, J.M., Modarres-Sadeghi, Y., Triantafyllou, M.S., 2014a. Coupled inline-cross flow VIV hydrodynamic coefficients database. In: ASME 2014 33rd International Conference on Ocean, Offshore and Arctic Engineering. American Society of Mechanical Engineers, pp. V002T08A087–V002T08A087.
- Zheng, H., Price, R.E., Modarres-Sadeghi, Y., Triantafyllou, M.S., 2014b. On fatigue damage of long flexible cylinders due to the higher harmonic force components and chaotic vortex-induced vibrations. *Ocean Eng.* 88, 318–329.